JOURNAL OF MECHANICAL ENGINEERING AND SCIENCES
ISSN: 2289-4659 e-ISSN: 2231-8380
VOLUME 20, ISSUE 2, 2026, 11178 - 11193
DOI: https://doi.org/10.15282/jmes.20.2.2026.4.0872

RESEARCH ARTICLE

Near-Wall double-bubble collapse dynamics and their impact-strengthening role in cavitation-assisted ultrasonic surface rolling

Hongbo Li, Jianxin Zheng*, Xiao Yu, Junhua Li, Yanyan Yan, Shen Niu

College of Mechanical & Power Engineering, Henan Polytechnic University, Jiaozuo 454003, Henan Province, China
Phone: +86-391-3987511

Abstract - Ultrasonic Surface Rolling (USR) is a surface deformation strengthening technology. By introducing cavitation effects into USR, the extreme high-pressure shock waves generated by the collapse of microscale bubbles can further enhance the surface strengthening effect. However, the synergistic mechanism governing near-wall double-bubble collapse in cavitation assisted USR remains unclear, limiting further optimization of the cavitation strengthening effect. This study investigates the dynamic behavior and synergistic mechanism of near-wall spherical double-bubble collapse in cavitation assisted USR through a combined numerical and experimental approach. A coupled dynamic model for spherical double bubbles and a shock wave pressure propagation model for the rolling region were developed and validated against cavitation assisted USR experiments. The results indicate that when double-bubble collapses, its synergistic effect increases the peak impact pressure by 23.6% compared to single-bubble. Analysis of the parameters reveals that the wall impact pressure is related to initial bubble radius, ultrasonic amplitude, dimensionless distance, and inter-bubble distance. This study has clarified the synergistic mechanism of the near-wall double-bubble collapse, providing theoretical support for controllably utilizing the cavitation effects in USR.

Article History
Received : 23 November 2025
Revised : 16 February 2026
Accepted : 9 June 2026
Published : 30 June 2026

Keywords
Ultrasonic surface rolling
Cavitation effect
Double-bubble
Shock wave pressure
Dynamical model

1. Introduction

High-end equipment imposes stringent performance requirements on parts, making surface strengthening technology critical for improving materials' resistance to wear, fatigue, and corrosion. Ultrasonic surface rolling (USR) is a severe plastic deformation technique for surfaces. It induces plastic deformation by combining high-frequency vibration impact with the static material surface, leading to gradient nanostructures and high compressive residual stress. USR demonstrates unique advantages in strengthening critical metal materials, including high-strength aluminium alloys [1], titanium alloys [2], magnesium alloys, and similar materials [3]. In USR, the cutting fluid in the rolling zone will induce significant cavitation effects under ultrasonic vibration excitation. The collapse of bubbles generates shock waves with peak pressures up to gigapascals, thereby inducing severe plastic deformation. If this phenomenon is utilised effectively, the material's surface microstructure can be controlled, thereby improving the service performance of parts [4]. Li et al. [5] reported that by introducing cavitation effects into USR treatment of 7075 aluminium alloy, finer grain size and higher compressive residual stress were formed in the surface layer of the specimen. This phenomenon was beneficial for improving material service performance. Chuai et al. [6] investigated the effect of ultrasonic cavitation at different frequencies on the surface quality of TC17 titanium alloy. Their results showed that the lower the vibration frequency, the greater the cavitation intensity. At 20 kHz, the maximum bubble radius reached up to 8.6 times the initial radius, while surface roughness decreased by 42.4% and microhardness increased by 10.8%, respectively. Chen et al. [7] performed ultrasonic cavitation treatments with varying exposure time. It was found that the treated surface became superhydrophobic and reduced the attachment of corrosion products. As a result, the self-corrosion current density and self-corrosion potential decreased by 93.9% and 21.0%, respectively, indicating improved corrosion resistance. Bai et al. [8] proposed an inner surface enhancement method based on cavitation utilisation. As a result, the surface hardness of stainless steel increased by approximately 12%, while the surface roughness remained largely unchanged. However, these works primarily focus on experimental phenomena and lack in-depth theoretical modelling of cavitation dynamics—especially for multi-bubble systems.

The study of cavitation effects began with the classical model [9]-[11]. Since cavitation typically occurs as multiple bubbles or bubble groups, the cavitation effect often arises from the group dynamics of these bubbles. The collapse of bubble groups not only involves the coupling effect between bubbles but also induces a superposition of the local stress field, producing more complex dynamic peening in the material. Alsaeed et al. [12] explored the collapse of a light square double-bubble, noting that the coupling strength between bubbles increases as the initial bubble distance decreases. However, square bubbles are uncommon, and they did not quantitatively analyse the interaction mechanism between cavitation bubbles. Zhao et al. [13] explored double-bubble collapse in the free domain. They reported that inter-bubble distance and bubble radius were negatively and positively correlated with the collapse-induced jet deflection angle, respectively. However, their analysis was limited to free-field conditions and did not consider the presence of a nearby wall. Hattori et al. [14] investigated multi-bubble collapse in the ultrasonic field. They found that higher pressure amplitudes increased outward mass transfer from the bubble interior. However, their study focused primarily on mass transfer rather than collapse-induced pressure. Liu et al. [15] investigated ultrasonically induced bubble clusters, demonstrating that an increase in the number of central bubbles and a decrease in their initial radius enhanced overall

*CORRESPONDING AUTHOR | Jianxin Zheng | ✉ zhengjx@hpu.edu.cn

cluster stability. Although they quantified the effects of interactions and parameters on bubble cluster collapse during bubble oscillation, they did not further investigate the collapse-induced pressure field and impact pressure. In ultrasonic machining, cavitation is a common phenomenon. However, the synergistic collapse mechanism of a double bubble in USR remains unclear, which limits effective regulation of the cavitation enhancement effect and the further development of process optimisation. In this study, a dynamic model of a spherical double bubble in the rolling zone is constructed and verified for cavitation-assisted USR. This study aims to investigate the influence of various processing parameters on the collapse behaviour of double-bubble, determine the intensity of shock waves from double-bubble collapse, and elucidate the mechanism of double-bubble collapse. This study lays the foundation for investigating the collapse laws and characteristics of bubble groups; meanwhile, it provides a theoretical basis for optimising USR processing parameters and regulating the cavitation impact-strengthening effect.

2. Materials and Methods

2.1 Principle of Cavitation-Assisted USR

The cavitation-assisted USR apparatus consists of an ultrasonic generator, transducer, horn, roller and a liquid supply system. The working principle of cavitation-assisted USR is shown in Figure 1. The roller advances axially at a feed rate of f_r, and the workpiece rotates at speed n. The roller applies rolling and high-frequency impact to the workpiece wall by synchronising longitudinal ultrasonic vibration with the static load F_s. In cavitation-assisted USR, the cutting fluid is supplied to the inner cavity of the horn and the rolling area. Due to ultrasonic waves, cavitation occurs in the cutting fluid around the roller [5], which further affects the surface, thereby enhancing the USR strengthening effect.

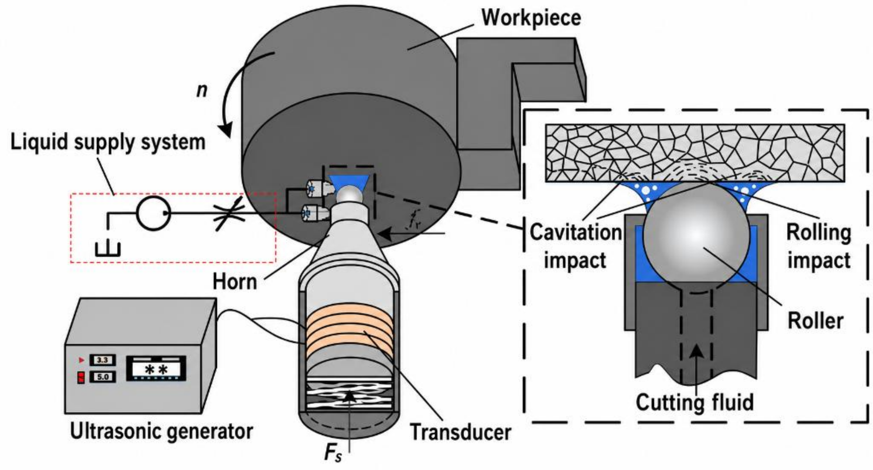

Figure 1. Schematic diagram of the principle of cavitation-assisted USR

2.2 Impact Pressure Model For Double-Bubble Collapse in Cavitation-Assisted USR

2.2.1 Dynamic model of single-bubble collapse

To investigate the impact of the shock wave from spherical bubble collapse in USR, the following simplifications and constraints are given (i) Gravity effect and energy dissipation are neglected. (ii) The bubble retains spherical morphology throughout periodic morphological changes, and its centre remains fixed. (iii) The bubble motion is limited to radial contraction, without relative motion to the surrounding fluid.

In USR, the total kinetic energy E_k of the bubble is the sum of the kinetic energy E_{k1} due to instantaneous radius change and the kinetic energy E_{k2} that is induced by the roller movement:

$$E_k = E_{k1} + E_{k2} = \frac{1}{2}M\dot{R}^2 + \frac{1}{2}Mv^2 \tag{1}$$

where M is the resonant mass of bubble, $M=4\pi\rho R^3$, and ρ is the surrounding liquid density and R is the bubble radius. $\dot{R}$ is the bubble wall velocity. The roller velocity v is given by $v=2\pi fA\cos(2\pi ft)$, where f is the ultrasonic vibration frequency, A is the vibration amplitude, and t is time.

When an external force causes the bubble to contract from its initial radius R_0 to radius R, the work W can be characterized as [16]:

$$W = -\int_{R_0}^{R} 4\pi P_{di} R^2 dR \tag{2}$$

where P_{di} is the pressure difference across bubble wall, which is dependent on the internal pressure P_{in} and external pressure P_{ex}, $P_{di}=P_{ex}-P_{in}$.

In USR, when the bubble with radius R is in equilibrium, its internal pressure P_{in} and external pressure P_{ex} can be expressed as [5], [17]:

$$P_{in} = P_v + P_g = P_v + (P_0 + 2\sigma/R_0)(R_0/R)^{3k} \tag{3}$$

$$P_{ex} = P_t + P_0 + 2\sigma/R + 4\mu\dot{R}/R \tag{4}$$

where P_v and P_g denote the vapor pressure and the gas pressure within the bubble, respectively. P_0 is the hydrostatic pressure of the liquid. k is the polytropic index, $k = 1.4$. $2\sigma/R$ is the surface tension term, with σ being the surface tension coefficient. $4\mu\dot{R}/R$ represents the viscous stress term, with μ being the liquid viscosity coefficient. $P_t = -P_A f(x)\sin 2\pi ft$ accounts for the driving acoustic pressure induced by the roller's motion, where $f(x)$ is the weighted function of acoustic pressure on the roller surface [18]. P_A signifies the acoustic pressure amplitude given by $P_A = 2\pi f\rho cA$, where c is the sound velocity in the liquid.

According to energy conservation, the work W from the pressure difference across the bubble equals the kinetic energy E_k acquired by the bubble, yielding:

$$\frac{1}{2}M\dot{R}^2 + \frac{1}{2}Mv^2 = -\int_{R_0}^{R} 4\pi P_{di} R^2 dR \tag{5}$$

Substituting P_{di} into Eq. (5) and differentiating, the single-bubble dynamic model in USR is obtained as:

$$\frac{3}{2}\dot{R}^2 + \frac{3}{2}v^2 + R\ddot{R} = \frac{1}{\rho}[P_v + (P_0 + 2\sigma/R_0)(R_0/R)^{3k} + P_A f(x)\sin 2\pi ft - P_0 - 2\sigma/R - 4\mu\dot{R}/R] \tag{6}$$

where $\ddot{R}$ is the bubble wall acceleration.

In USR, the workpiece wall can be treated as rigid. When ultrasonic waves reach a rigid wall, they are reflected. Therefore, under rigid-wall conditions, the dynamics of a spherical bubble are influenced by both incident and reflected waves [19]. Based on the mirror image rule, this boundary reflection effect can be equivalently described by wavefield interference from a mirrored bubble. The mirrored cavitation system formed by ultrasonic reflection near the rigid wall is illustrated in Figure 2.

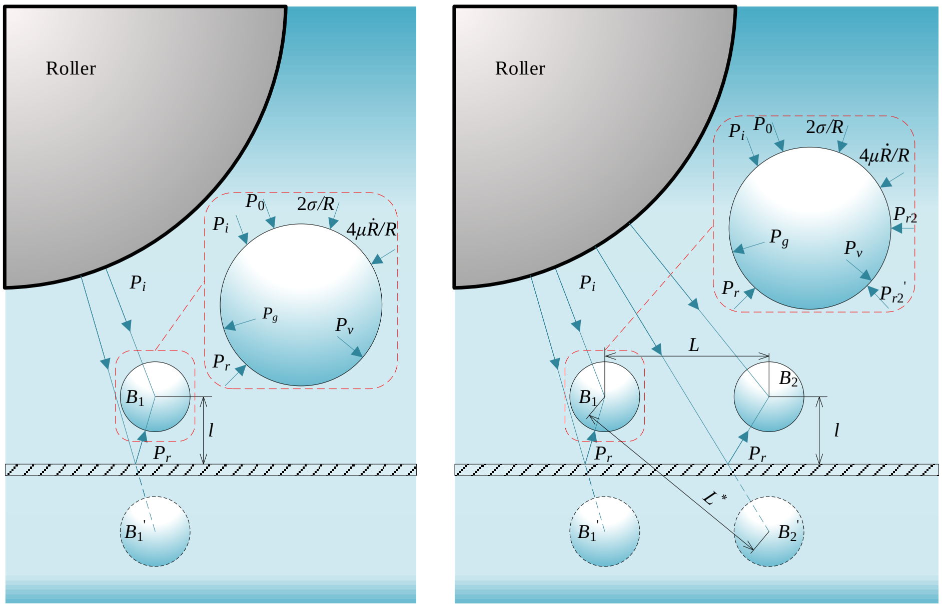

(a) Single-bubble (b) Double-bubble

Figure 2. Mirrored cavitation system near a rigid wall with wave reflection effects

In the single-bubble mirrored cavitation system shown in Figure 2(a), the actual bubble B_1 has radius R_1, centred at O_1, while the mirrored bubble B_1' has radius R_1', centred at O_1'. The distance from the centres of both bubbles to the workpiece wall is l. Both bubbles maintain equal radii, i.e., $R_1 = R_1' = R$.

According to the acoustic reflection law, the acoustic pressure of the incident wave P_i and reflected wave P_r are expressed as [20]:

$$P_i = P_{iA} f(x)\sin(2\pi ft + \beta_i l) \tag{7}$$

$$P_r = P_{rA} f(x)\sin(2\pi ft + \beta_r l) \tag{8}$$

where β_i and β_r are the wavenumbers of incident and reflected waves respectively, and $\beta_i = \beta_r = 2\pi f/c$. P_{iA} and P_{rA} are the acoustic pressure amplitudes of the incident wave and reflected wave, respectively.

In USR, the ultrasonic wave undergoes total reflection at rigid walls. Since the actual bubble is located on the micrometre scale from the workpiece surface, the acoustic pressure amplitudes of the incident and reflected waves remain nearly identical. Therefore:

$$P_i = P_r = P_t \tag{9}$$

Considering the influence of mirrored bubble B_1', the external pressure in Eq. (4) needs to be revised to:

$$P_{ex} = P_i + P_r + P_0 + 2\sigma/R + 4\mu\dot{R}/R \tag{10}$$

Therefore, in near-wall conditions when accounting for reflected wave influence, the dynamic model of a single-bubble in USR becomes:

$$\frac{3}{2}\dot{R}^2 + \frac{3}{2}v^2 + R\ddot{R} = \frac{1}{\rho}[P_v + (P_0 + 2\sigma/R_0)(R_0/R)^{3k} + 2P_A f(x)\sin(2\pi f t + \beta_i l) - P_0 - 2\sigma/R - 4\mu\dot{R}/R] \tag{11}$$

2.2.2 Dynamic model of double-bubble collapse

Figure 2(b) shows that the actual bubbles B_1 and B_2 have radii R_1 and R_2 and centre positions O_1 and O_2, respectively. And their mirrored bubbles B_1' and B_2' have radii R_1', R_2' and centre positions O_1', O_2', respectively. The horizontal inter-bubble distance is L. Assuming the distance from each bubble's centre to the workpiece wall is l. The actual and mirrored bubbles have equal radii, i.e., $R_1 = R_1'$, $R_2 = R_2'$.

The velocity potential φ at point A located at a distance s from an oscillating bubble's centre is expressed as [21]:

$$\varphi = R^2\dot{R}/s^2 \tag{12}$$

The pressure P_e radiated into the surrounding liquid by an oscillating bubble is [22]:

$$\frac{\partial\varphi}{\partial t} + \varphi\frac{\partial\varphi}{\partial s} = \frac{1}{\rho}\frac{\partial P_e}{\partial s} \tag{13}$$

Substituting Eq. (12) into Eq. (13) and integrating over s, we obtain:

$$P_e = \rho[(2R\dot{R}^2 + R^2\ddot{R})/s - R^4\dot{R}^2/2s^4] \tag{14}$$

Once the bubble's instantaneous radius reaches its minimum R_{min}, collapse occurs. Consequently, the impact pressure P_s generated during collapse can be derived from Eq. (14), where $P_s = P_e$ at $R = R_{min}$.

Bubble B_1 experiences not only the pressure P_r from mirrored bubble B_1', but also the radiation pressure P_{r2} from bubble B_2 and P_{r2}' from mirrored bubble B_2'. Based on Eq. (14), these pressures are formulated as:

$$P_{r2} = \rho[(2R_2\dot{R}_2^2 + R_2^2\ddot{R}_2)/L - R_2^4\dot{R}_2^2/2L^4] \tag{15}$$

$$P_{r2}' = \rho[(2R_2\dot{R}_2^2 + R_2^2\ddot{R}_2)/L^* - R_2^4\dot{R}_2^2/2L^{*4}] \tag{16}$$

where $L^* = \sqrt{L^2 + 4l^2}$.

Therefore, the external pressure P_{ex1} acting on bubble B_1 must be modified to:

$$P_{ex1} = P_i + P_r + P_{r2} + P_{r2}' + P_0 + 2\sigma/R + 4\mu\dot{R}/R \tag{17}$$

This leads to the dynamic model for bubble B_1 near the rigid wall in a double-bubble environment in USR:

$$\begin{aligned}\frac{3}{2}\dot{R}_1^2 + \frac{3}{2}v^2 + R_1\ddot{R}_1 + \frac{2R_2\dot{R}_2^2 + R_2^2\ddot{R}_2}{L} - \frac{R_2^4\dot{R}_2^2}{2L^4} + \frac{2R_2\dot{R}_2^2 + R_2^2\ddot{R}_2}{L^*} - \frac{R_2^4\dot{R}_2^2}{2L^{*4}} \\ = \frac{1}{\rho}[P_v + (P_0 + \frac{2\sigma}{R_{10}})\left(\frac{R_{10}}{R_1}\right)^{3k} + 2P_A f(x)\sin(2\pi f t + \beta_i l) - P_0 - \frac{2\sigma}{R_1} - \frac{4\mu\dot{R}_1}{R_1}]\end{aligned} \tag{18}$$

where R_{10} and R_{20} are the initial radii of bubbles B_1 and B_2, respectively.

The dynamic model for bubble B_2 is derived similarly:

$$\begin{aligned}\frac{3}{2}\dot{R}_2^2 + \frac{3}{2}v^2 + R_2\ddot{R}_2 + \frac{2R_1\dot{R}_1^2 + R_1^2\ddot{R}_1}{L} - \frac{R_1^4\dot{R}_1^2}{2L^4} + \frac{2R_1\dot{R}_1^2 + R_1^2\ddot{R}_1}{L^*} - \frac{R_1^4\dot{R}_1^2}{2L^{*4}} \\ = \frac{1}{\rho}[P_v + (P_0 + \frac{2\sigma}{R_{20}})\left(\frac{R_{20}}{R_2}\right)^{3k} + 2P_A f(x)\sin(2\pi f t + \beta_i l) - P_0 - \frac{2\sigma}{R_2} - \frac{4\mu\dot{R}_2}{R_2}]\end{aligned} \tag{19}$$

2.2.3 Pressure model induced by bubble collapse

The bubbles shrink and collapse rapidly under the action of the flow field pressure. The energy accumulated in the bubbles is released instantaneously. This release strongly squeezes the surrounding liquid medium. Thus, a high-speed shock wave propagates through the liquid. For a single-bubble environment, when the instantaneous radius attains its minimum ($R = R_{\min}$), the resulting shock wave pressure P_s is given by:

$$P_s = \rho[(2R\dot{R}^2 + R^2\ddot{R})/s - R^4\dot{R}^2/2s^4] \tag{20}$$

At this stage, in a single-bubble system, the pressure P_c at point A (located at distances s from the bubble center) comprises three components: the driving acoustic pressure P_t, the hydrostatic pressure P_0, and the shock wave pressure P_s [5]. Since this study focuses on the impact pressure generated by bubble collapse on the wall, the wall reflection of the shock-wave pressure P_s is neglected. So, the pressure P_c can be expressed as:

$$P_c = P_A f(x)\sin 2\pi f t + P_0 + \rho[R^2\ddot{R}/s + 2\dot{R}^2(R/s - R^4/4s^4)] \tag{21}$$

Similarly, in a double-bubble system, the total pressure P_{total} at point A (with distance s_1 and s_2 from the centers of bubbles B_1 and B_2 respectively) constitutes the driving acoustic pressure P_t, the hydrostatic pressure P_0, the shock wave pressures P_{s1} and P_{s2} from bubbles B_1 and B_2 collapse:

$$\begin{gathered} P_{total} = P_A f(x)\sin 2\pi f t + P_0 + P_{s1} + P_{s2} \\ = P_A f(x)\sin 2\pi f t + P_0 + \rho[R_1^2\ddot{R}_1/s_1 + 2\dot{R}_1^2(R_1/s_1 - R_1^4/4s_1^4)] + \rho[R_2^2\ddot{R}_2/s_2 + 2\dot{R}_2^2(R_2/s_2 - R_2^4/4s_2^4)] \end{gathered} \tag{22}$$

2.3 Numerical Computation Method and Parameters

To quantify the shock-wave effects of spherical bubble collapse on the workpiece wall, this work analysed the bubble dynamics and pressure models established above. These second-order nonlinear ordinary differential equations cannot be solved analytically and therefore require numerical solutions using the fourth-order Runge-Kutta method. The computation parameters are listed in Table 1. The dimensionless distance is defined as $\gamma = l/R_0$, where l is the bubble-wall distance, and R0 is the initial bubble radius. The initial bubble radius typically ranges from 1 μm to 200 μm [23], [24]. The initial bubble radius is selected as 10 μm to 40 μm in this study. In a previous study of single cavitation bubble collapse, the amplitude was set to 2-5 μm [25]. However, this amplitude leads to a low probability of double-bubble cavitation collapse, making observation difficult. To enhance the intensity of the cavitation effect, an amplitude range of 3-6 μm is adopted in the present study. When γ >1.5, cavitation bubbles collapse in a spherical form, and the wall surface is mainly affected by the bubble shock wave during collapse [26]. Therefore, the value of γ is selected to be in the range of 1.5 to 3. The commonly used inter-bubble distance ranges from 3 to 15 times the initial bubble radius [14], [27]. Therefore, this study adopts a range of 6 to 12 times the initial bubble radius, i.e., 60–120 μm.

Table 1. Computation parameters

Parameters	Values
initial bubble radius R_0=R_{10}=R_{20} / μm	10-40
ultrasonic amplitude A / μm	3-6
dimensionless distance $\gamma = \gamma_1 = \gamma_2$	1.5-3
inter-bubble distance L / μm	60-120
hydrostatic pressure P_0 / MPa	0.1013
ultrasonic vibration frequency f / kHz	24.14
liquid density ρ / Kg/m^3	1000
viscosity coefficient μ / Kg/(m·s)	0.001
surface tension coefficient σ / N/m	0.0725
sound velocity in the liquid c / m/s	1500

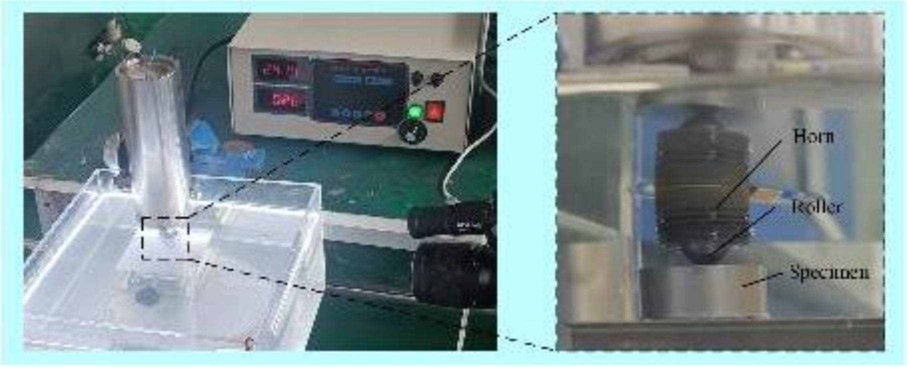

Figure 3. Ultrasonic cavitation experimental device

2.4 Experiment

By performing inverse analysis of the cavitation erosion surface morphology, this study investigated cavitation mechanisms and all impact pressures to validate the dynamics model of near-wall bubble collapse in USR. Critically, under current experimental conditions, key parameters governing cavitation—including initial bubble radius, dimensionless distance, and inter-bubble spacing -cannot be actively controlled or precisely measured. Therefore, the cavitation erosion tests specifically examined the effect of ultrasonic amplitude on wall impact pressure. The USR cavitation test system, illustrated in Figure 3, operated at a vibration frequency of 24.14 kHz. The schematic diagram of the horn used in this study is illustrated in Figure 4. The horn transmits vibrations to the roller, which radiates sound pressure into liquid, thereby generating cavitation and forming cavitation pits on the specimen surface. The test specimens were commercial 1060 aluminium alloy. Before cavitation testing, the specimens were polished to obtain smooth, flat, defect-free surfaces. The polished and cavitation erosion surfaces were characterised using a VHX-2000 ultra-depth 3D microscope.

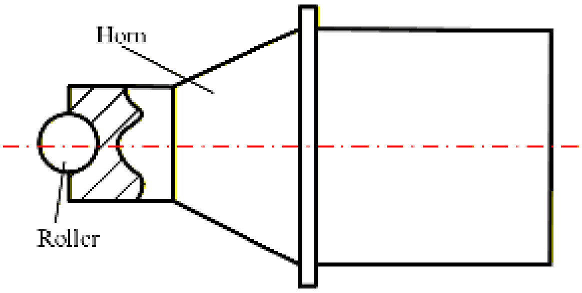

Figure 4. Schematic diagram of the horn

3. Results and Discussion

3.1 Validation of the Theoretical Model

This section analyses the validation of the theoretical model by comparing the analytically predicted wall impact pressures with values obtained by inverse calculation from experimental cavitation morphologies. The characteristics of cavitation erosion pits in single-bubble and double-bubble environments are analysed, and the accuracy and applicable limitations of the theoretical model are discussed. Figure 5(a) shows the absence of pits or other defects after polishing. Distinct erosion pits observed in Figure 5(b) confirm cavitation-induced damage. The shock wave generated by spherical bubble collapse produces flatter cavitation pits on the material surface, while the microjet from non-spherical collapse creates deeper, needle-like pits [25], [28]-[29]. So, we included only cavitation pits that exhibited typical spherical collapse features, ensuring reliable data.

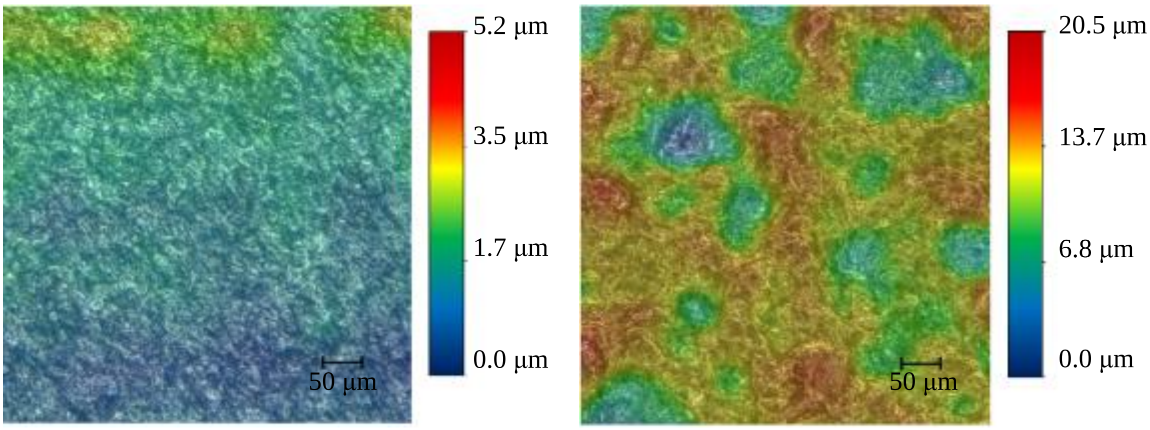

(a) After polishing (b) After cavitation erosion

Figure 5. Surface morphology of the specimen after polishing and cavitation erosion

Figure 6 shows the cavitation erosion pits on the surface of the specimen. Most of these pits are circular or nearly circular in shape, with smooth and symmetrical cross-sections. They are distributed sparsely without any clustering. This is characteristic of single-bubble spherical collapse [30]. If a double-bubble collapses due to the influence of pressure fields, asymmetric impacts will occur, resulting in pits that take on elliptical or irregular shapes [31]. To ensure the reliability of the results, we only analyse the pits caused by bubbles with clearly defined shapes. In Figure 6, single-bubble pits are enclosed by dashed circles, while dash-dotted boundaries identify double-bubble pits.

The relationship between the wall impact pressure P_{wall} and the diameter d and depth h of erosion pits generated by spherically collapsing bubbles is expressed as [5]:

$$P_{wall} = \psi\sigma_y[\frac{4dh}{5\varepsilon_y(d^2+4h^2)}]^n \tag{23}$$

where ψ is the constraint coefficient, taken as 2.87; σ_y denotes the yield stress, set to 20 MPa; ε_y represents the strain at yield onset, set to 0.2%, and n is the strain hardening exponent, set to 0.23.

Based on Eq. (23), the wall impact pressures were inversely calculated from cavitation erosion measurements. Figure 7 compares inverse-derived and analytically predicted maximum wall-impact pressures at different amplitudes in single-bubble and double-bubble environments. The legend for Figure 7 is explained as follows: Sin-Exp is the inverse-calculated pressure in a single-bubble environment, Sin-Ana is the analytically predicted maximum wall pressure in a single-bubble environment, Dou-Exp is the inverse-calculated pressure in a double-bubble environment, and Dou-Ana is the analytically predicted maximum wall pressure in a double-bubble environment.

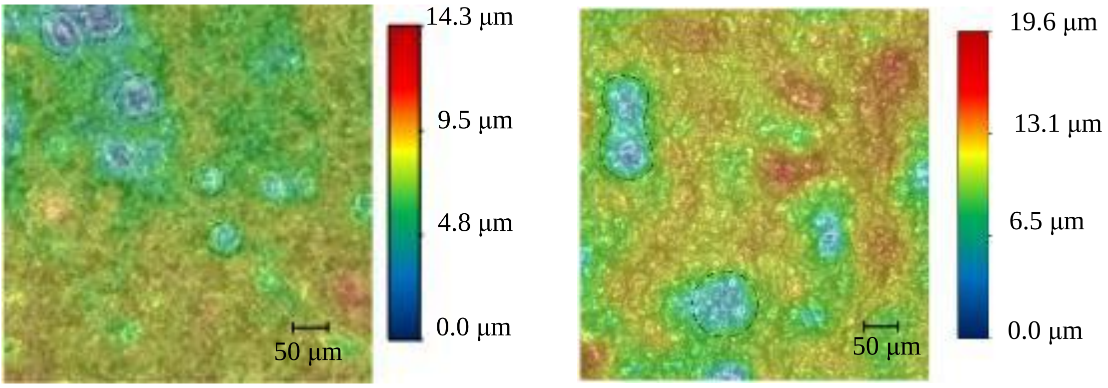

(a) A=3 μm (b) A=4 μm

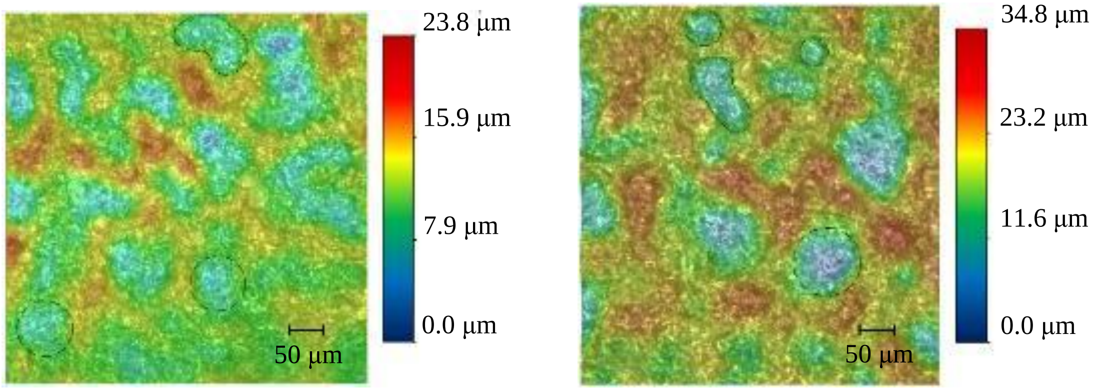

(c) A=5 μm (d) A=6 μm

Figure 6. Morphology of cavitation erosion pits under different amplitudes

Analytical predictions for pressure beneath bubble B_1 (Eqs. 21 and 22) assumed: the initial bubble radius R_{10}=R_{20}=10 μm, the dimensionless distance γ_1=γ_2=1.5, and the inter-bubble distance L=100 μm. For a fixed ultrasonic amplitude A with other parameters held constant, the analytically predicted maximum wall pressures in both single-bubble and double-bubble environments remain invariant, manifesting as horizontal planes in Figure 7. Figure 7 shows that at identical amplitudes, double-bubble collapse generates 12.6–23.6% higher experimental wall impact pressures, P_{wall}, than single-bubble collapse, and that increasing A monotonically elevates P_{wall} in both configurations. When A=4 μm, the pressure increases by a maximum of 23.6% (P_{wall} rose from 301.4 MPa to 394.5 MPa), while it shows a minimum increase of 12.6% at A=3 μm (P_{wall} rose from 211.8 MPa to 238.7 MPa). These data demonstrate a pressure superposition phenomenon during double-bubble collapse. Across all ultrasonic amplitudes, the maximum relative error of analytically predicted values is 15.6%, with minimum and average errors of 6.2% and 11.1%, respectively. At amplitudes of 3, 4, 5, and 6 μm, the maximum errors between analytically predicted and inversely calculated values are 12.7%, 15.6%, 13.2%, and 9.7% for single-bubble environments. For double-bubble environments, those numbers are 11.2%, 11.0%, 9.8%, and 6.2%. This level of error suggests that bubble dynamics and pressure field models are reliable. Figure 7 shows that the wall pressure values obtained experimentally are higher than those predicted by the theoretical model under the same conditions. This difference is mainly due to the omission of secondary Bjerknes forces in the bubble dynamics model. In addition, the following five limitations may also be sources of error. The theoretical model is based on simplified assumptions: incompressible liquids and isolated spherical bubbles in free-flow fields. This leads to systematic deviations because it fails to fully capture the complexity of bubble-collapse behaviour. Factors such as the content of non-gelatinous gases and interactions among multiple bubbles are not taken into account. As a result, the theoretical pressure values are underestimated. The theoretical model neglects the attenuation during wave propagation and boundary reflection. Consequently, the simulated impact pressure deviates from the actual working conditions to some extent. This model assumes that bubble collapse is spherical. However, actual bubbles undergo non-spherical collapse due to boundary effects and flow asymmetries, thus affecting the modelling accuracy. The theoretical model adopts an idealised double-bubble configuration with identical radii and symmetric wall distances. Such conditions are rarely met in experiments, which introduces errors.

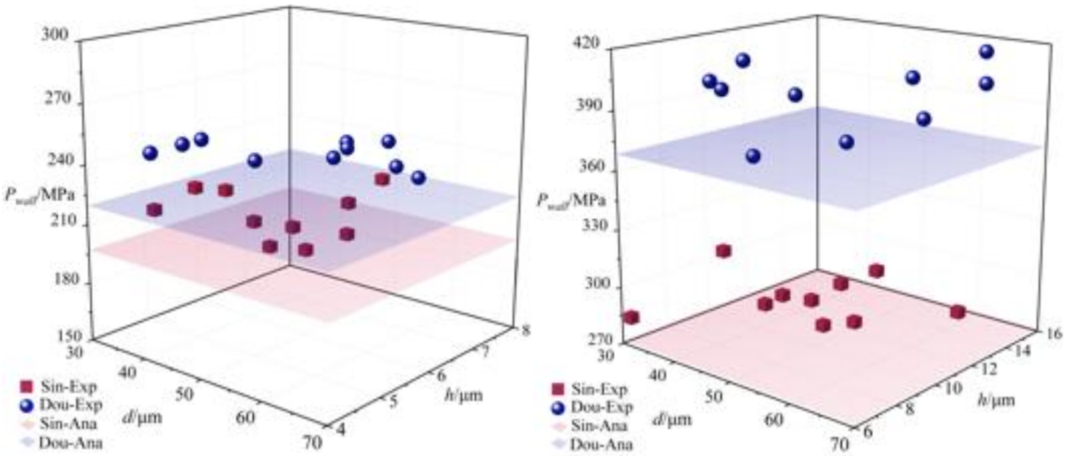

(a) A=3 μm (b) A=4 μm

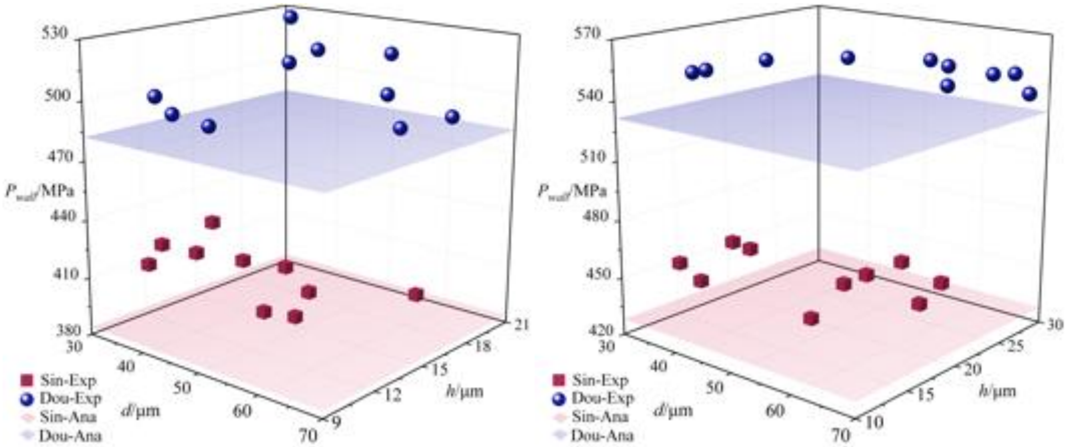

(c) A=5 μm (d) A=6 μm

Figure 7. Inverse-derived and analytically predicted wall pressure under different amplitudes

3.2 Influence of Initial Bubble Radius

Under different initial radii, bubbles exhibit distinct dynamic characteristics under ultrasonic excitation. In the numerical computation, the ultrasonic amplitude was 5 μm. In the single-bubble environment, the initial bubble radius R_0 was set to 10, 20, 30, and 40 μm, and the dimensionless distance γ was set to 1.5. In the double-bubble environment, the initial radii R_{10} and R_{20} were set to 10, 20, 30, and 40 μm; meanwhile, the dimensionless distances γ_1 and γ_2 of bubbles B_1 and B_2, respectively, were set to 1.5, with an inter-bubble distance L of 100 μm. Figure 8 compares the radius ratios R/R_0 and R_1/R_{10} for bubble B_1 in the single-bubble and double-bubble environments.

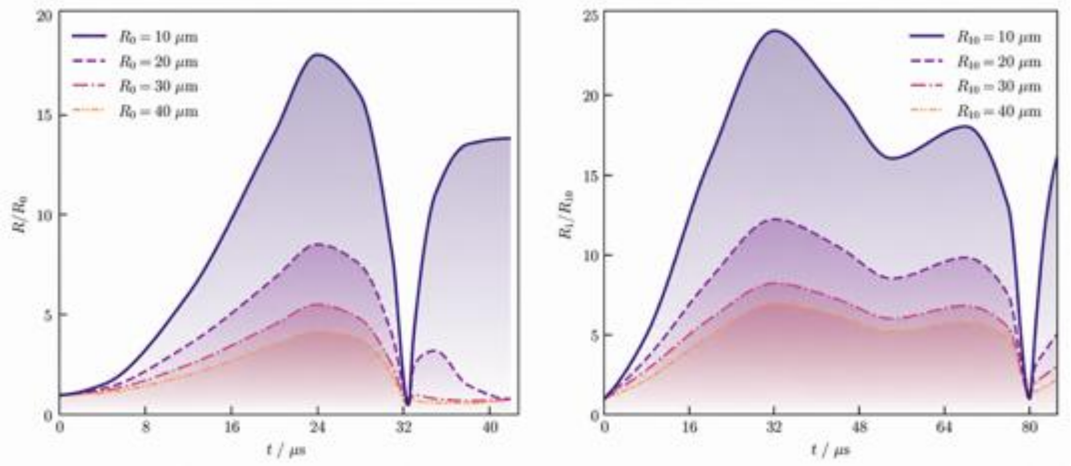

(a) Single-bubble environment (b) Double-bubble environment

Figure 8. Evolution of bubble radius ratio at various initial radii

Figure 8 shows that the radius ratio is inversely related to the initial radius. In a single-bubble environment at R_0=40 μm, the minimum-radius-ratio peak is 4.1, which is 22.6% of that at R_0=10 μm. In a double-bubble environment, at R_{10}=40 μm, the minimum radius ratio peak is 6.9, which is 28.7% of that at R_{10}=10 μm. Moreover, the radius ratio of bubble B_1

in the double-bubble environment is greater under the same parameters. This finding is consistent with the results reported by Luo et al. [32]. When R_{10}=10 μm, the maximum radius ratio in the double-bubble environment reaches 23.9, which is 31.8% higher than in the single-bubble environment. The larger the initial radius, the smaller the radius ratio, because the resonant mass increases accordingly. With the same amount of energy applied, a larger resonant mass results in smaller radial acceleration. As a result, the expansion and contraction become less pronounced, causing a smaller variation in the radius ratio. Besides, the external forces acting on bubble B_1 are greater in a double-bubble environment, thus the radius ratio varies more drastically. In a double-bubble environment, bubble B_1 is not only affected by fundamental acoustic pressure and the radiation pressure from the mirrored bubble B_1', but also experiences radiation pressures from the adjacent bubble B_2 and its mirrored bubble B_2'. With these combined pressures, the force field becomes stronger, and the change in radius ratio is also greater. A larger radius ratio means the shock-wave pressure generated when the bubble breaks is higher. Therefore, in a double-bubble environment, the shock wave generated may be stronger.

As shown in Figure 8, the double-bubble environment results in both a prolonged oscillation period and a dual-peak pattern, matching the findings of Yang et al. [33] and Liu et al. [34]. When the initial radius is 40 μm, the double-bubble system attains a maximum oscillation period of 82.8 μs. This value is 153.9% higher than the 32.6 μs observed in the single-bubble system. The dual-peak phenomenon arises from a reversal of the dynamic pressure gradient. In a double-bubble environment, after bubble B_1 reaches its first maximum radius, the radiation pressures P_{r2} and P_{r2}' progressively drop and eventually become negative. Thus, B_1's external pressure becomes lower than its internal pressure. This gradient causes the bubble to re-expand, creating the dual-peak pattern and thereby extending the oscillation period. Figure 8 further shows that an increase in the initial bubble radius reduces the collapse time in the single-bubble environment but extends it in the double-bubble environment. These findings are consistent with those of Yang et al. [35] and Zhang et al. [36]. In a single-bubble environment, increasing the initial radius of bubble B_1 enhances hydrodynamic instability, which in turn accelerates the collapse. Before collapsing in a double-bubble environment, both bubbles undergo fast contraction. The contraction of bubble B_2 induces a negative-pressure field. This field decreases the external pressure on bubble B_1. Increasing the initial radius of B_2 amplifies this negative-pressure effect, causing an even greater reduction in external pressure on B_1 and leading to delayed collapse time.

Figures 9(a) and 9(b) show the pressure field distributions produced by the collapse of bubble B_1 in single-bubble and double-bubble environments. To comparatively analyse pressure field variations, Figure 9 integrates quadrant sections at different initial radii into a unified coordinate framework. Figure 9 shows that, in both single-bubble and double-bubble environments, a larger initial bubble radius leads to lower collapse-induced pressure. As shown in Figure 8, smaller initial radii in both environments lead to more violent radius-ratio oscillations. These more violent oscillations elevate both the bubble wall velocity and acceleration. Thus, the increased speed of bubble collapse leads to higher shock-wave pressure. Figure 9 also demonstrates that, with identical initial radii, the double-bubble system produces a stronger shock-wave pressure. Figure 8 demonstrates that the double-bubble environment exhibits more dramatic variations in radius ratio. These variations produce a greater pressure upon collapse. Figure 9 further reveals a characteristic non-monotonic pressure distribution along radial paths from the bubble centre: pressure initially increases, then decreases. This is attributed to the outward displacement of the fluid at the original bubble centre driven by post-collapse fluid motion [25]. This displacement creates a low-pressure region at the collapse origin, while the propagating shock pressure decays with radial distance [37]. Consequently, the shock pressure peaks at intermediate radial positions before attenuating. Similar phenomena have been reported by Yang et al. [38] and Choi et al. [39]. The collapse-induced shock pressure on the workpiece wall directly below bubble B_1 is defined as the wall impact pressure P_{wall}. To simplify the analysis, the configuration in a double-bubble environment is restricted to a symmetric case in which both bubbles are equidistant from the wall. Figure 10(a) and 10(b) compare P_{wall} values across different initial bubble radii for the single-bubble and double-bubble environments, respectively.

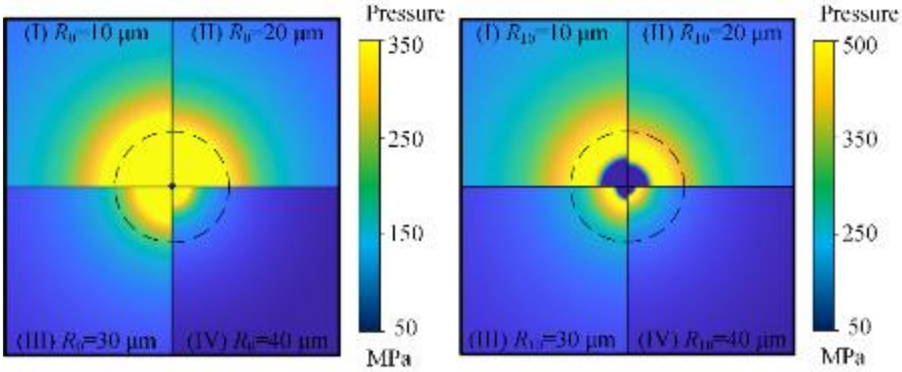

(a) Single-bubble environment (b) Double-bubble environment

Figure 9. Pressure field generated by bubble B_1's collapse at different initial radii

Figure 10 shows that the wall impact pressure P_{wall} decreases as the initial bubble radius increases. In a single-bubble environment, at R_0=10 μm, the maximum P_{wall} is 383.8 MPa, which is 4.1 times that at R_0=40 μm. In a double-bubble environment, at R_{10}=10 μm, the maximum P_{wall} is 482.3 MPa, which is 3.15 times the value at $R_{10=40}$ μm. Besides, P_{wall} in the double-bubble environment are consistently higher. At an initial radius of 10 μm, the maximum P_{wall} is 482.3 MPa in the double-bubble environment, representing a 20.4% increase. As established, smaller initial radii generate higher collapse pressures. Since P_{wall} represents collapse-induced shock pressure at the workpiece wall beneath bubble B_1, it exhibits relatedinversely inverse to the initial radius. Similarly, the elevated collapse pressures in the double-bubble environment correspondingly increase P_{wall} relative to the single-bubble environment.

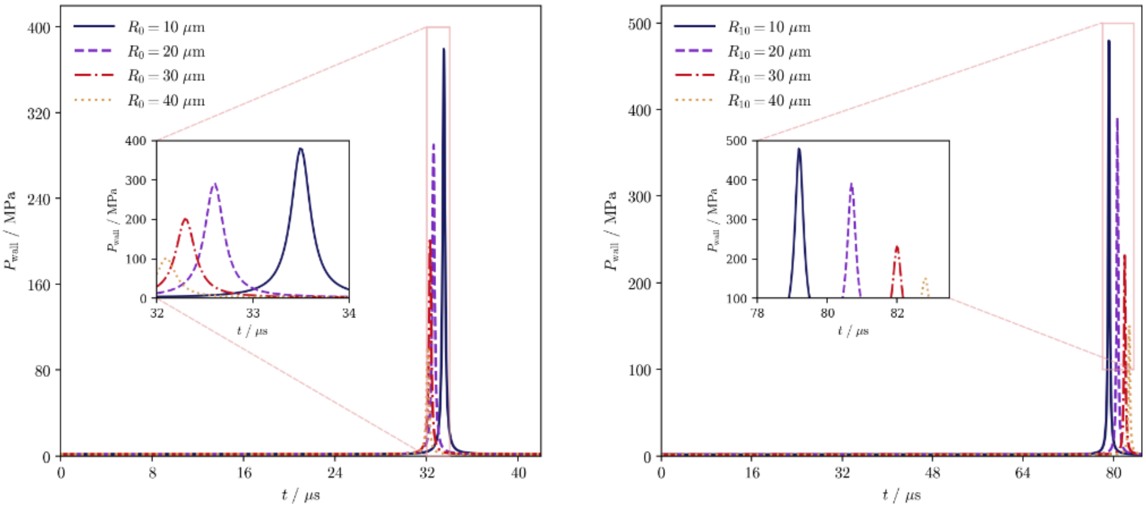

(a) Single-bubble environment (b) Double-bubble environment

Figure 10. Wall impact pressure at different initial bubble radii

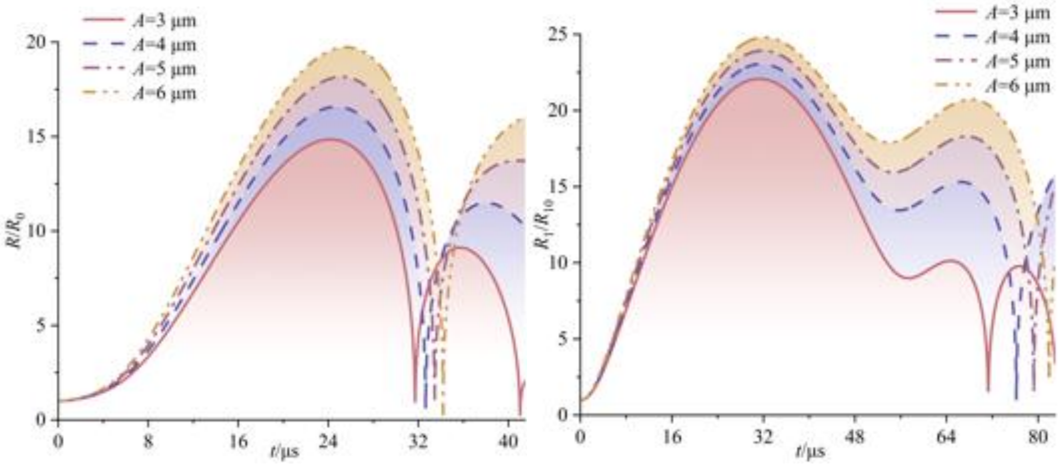

(a) Single-bubble environment (b) Double-bubble environment

Figure 11. Evolution of bubble radius ratio at different amplitudes

3.3 Influence ff Ultrasonic Amplitude

Under different ultrasonic amplitudes, bubbles exhibit distinct cavitation behaviours due to varying energy input. In the numerical computation, the initial bubble radius was set to 10 μm, the ultrasonic amplitudes to 3, 4, 5, and 6 μm, and the dimensionless distance to 1.5. In the double-bubble environment, the inter-bubble distance was set to 100 μm. Figure 11 shows the variation of the radius ratio R/R_0 and R_1/R_{10} for bubble B_1 at different ultrasonic amplitudes. Figure 11 shows that as the ultrasonic amplitude increases, the maximum bubble radius ratio also increases. In a single-bubble environment at A=6 μm, the maximum radius ratio reaches 19.7 (a 32.9% increase from A=3 μm), while in a double-bubble environment it reaches 24.8 (a 12.4% increase from A=3 μm). As the ultrasonic amplitude increases, the horn radiates greater acoustic pressure, thereby increasing the external pressure on the bubble. The resulting larger pressure difference between the inside and outside of the bubble intensifies the mechanical work acting on the bubble wall. Enhancing this mechanical work effectively increases the bubble wall velocity and acceleration, making the bubble oscillations more vigorous. This is directly reflected in the positive correlation between ultrasonic amplitude and bubble radius ratio. Furthermore, under the same amplitude, bubble B_1 exhibits more pronounced radius ratio variations in a double-bubble environment. At A = 6 μm, the peak radius ratio in a dual-bubble environment reaches 24.8, an increase of 25.7% compared to that in a single-bubble environment. As discussed in Section 3.2, the greater variation in radius ratio in the double-bubble environment stems from the higher external pressure compared to the single-bubble environment. Subsequent references to larger radius ratios in the double-bubble environment are attributed to this same cause and will not be reiterated. Figure 11 further indicates that under identical parameters, the oscillation period is significantly prolonged in the double-bubble environment, where the dual-peak phenomenon also occurs. As the extended oscillation period and dual-peak phenomenon in the double-bubble environment have been explained previously, their causes will not be reiterated here or subsequently.

Figures 12(a-b) show the collapse-induced pressure fields of bubble B_1 at various ultrasonic amplitudes in the single-bubble and double-bubble environments. Figure 12 demonstrates that collapse-induced pressure increases with ultrasonic amplitude in both single-bubble and double-bubble environments. For a given initial radius, the shock-wave pressure is higher in the double-bubble environment. Figure 11 reveals that larger amplitudes in the single-bubble environment amplify oscillations of radius ratio, indicating higher bubble wall velocity and acceleration. Higher velocity and acceleration indicate more violent bubble oscillations, resulting in greater shock-wave pressure at the moment of collapse. Given that the causes of the higher collapse-induced pressure in the double-bubble environment have already been addressed, they are not reiterated.

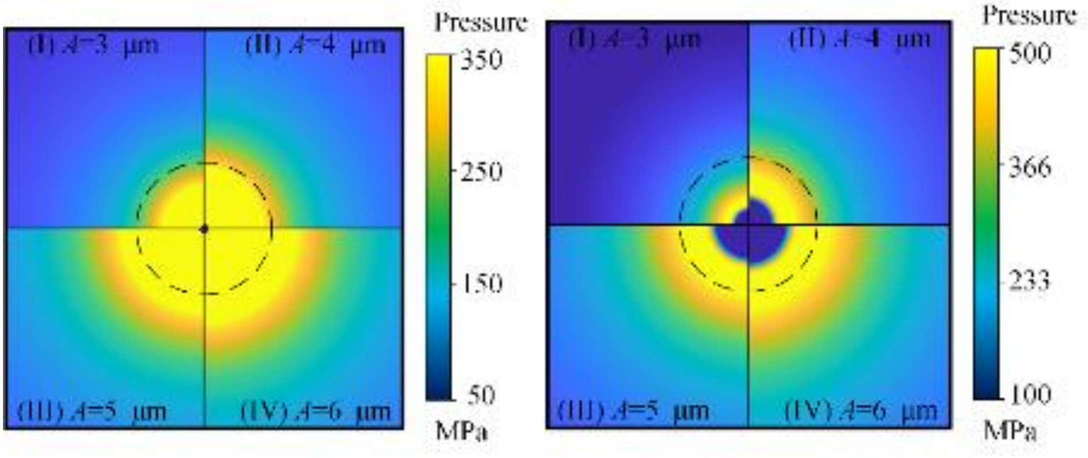

(a) Single-bubble environment (b) Double-bubble environment

Figure 12. Pressure field generated by bubble B_1's collapse at different ultrasonic amplitudes

Figures 13(a-b) present wall impact pressure under different ultrasonic amplitudes in the single-bubble and double-bubble environments, respectively. Figure 13 reveals that the wall impact pressure P_{wall} increases with ultrasonic amplitude A. In a single-bubble environment, at A=6 µm, the maximum P_{wall} is 428.0 MPa, which is 2.2 times that at A=3 µm. In a double-bubble environment, at A=6 µm, the maximum P_{wall} is 531.6 MPa, which is 2.4 times that at A=3 µm. Furthermore, P_{wall} in the double-bubble environment are consistently higher. At 6 µm amplitude, the maximum P_{wall} is 531.6 MPa in the double-bubble environment, representing a 19.5% increase. As mentioned previously, higher ultrasonic amplitudes and the double-bubble environment produce higher collapse pressure. Since P_{wall} represents collapse-induced pressure at the workpiece wall beneath bubble B_1, it consequently exhibits a positive correlation with ultrasonic amplitude. Moreover, P_{wall} in the double-bubble environment are consistently higher than that in the single-bubble environment.

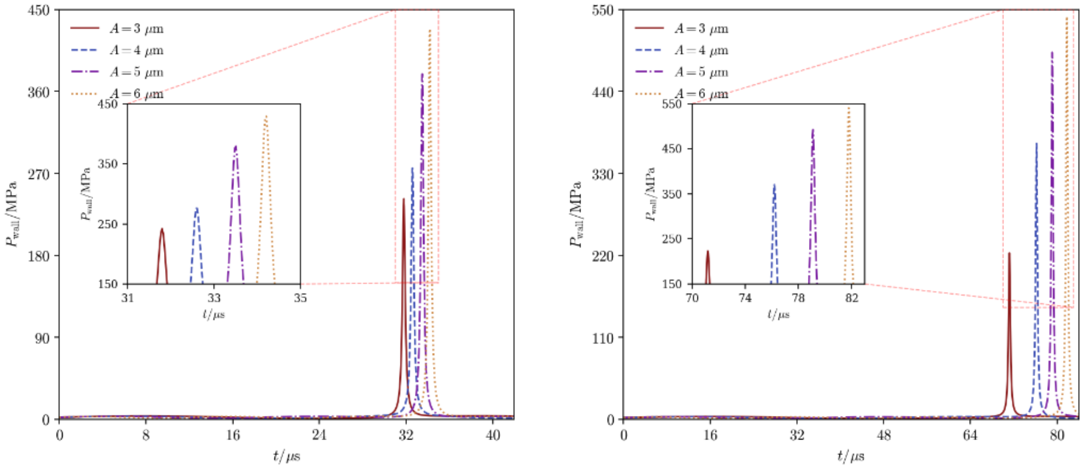

(a) Single-bubble environment (b) Double-bubble environment

Figure 13. Wall impact pressure at different ultrasonic amplitudes

3.4 Influence of Dimensionless Distance

A larger dimensionless distance increases the separation between the bubble and the wall. This change in spacing modifies the characteristics of reflected waves, which in turn affects bubble dynamics and the distribution of collapse-induced pressure fields. Set the initial bubble radius R_0=R_{10}=R_{20}=10 µm, the ultrasonic amplitude A=5 µm, and the dimensionless distance γ = γ_1= γ_2 =1.5, 2.0, 2.5, and 3.0. In the double-bubble environment, the inter-bubble distance was set to L=100 μm. Figure 14 depicts the variation of the radius ratio R/R_0 and R_1/R_{10} for bubble B_1 at different dimensionless distance values. Figure 14 demonstrates that the bubble radius ratio increases with larger dimensionless distance. In a single-bubble environment, at γ=3.0, the radius ratio peak reaches a maximum of 21.5, an increase of 18.2% compared to that at γ=1.5. In a double-bubble environment at γ_1=3.0, the radius ratio peak reaches a maximum of 28.1, an increase of 17.5% over that at γ_1=1.5. When the initial radius is fixed, an increase in the dimensionless distance corresponds to a greater bubble-wall distance. In the near-wall region, the phase difference between the incident wave and the reflected wave often leads to wave crest–trough cancellation, which weakens the internal-external pressure difference across the bubble wall, consequently inhibiting bubble oscillation. As the bubble-wall distance increases, this weakening effect diminishes, resulting in a negative correlation between the dimensionless distance and the radius ratio. In Figure 14, under the same dimensionless distance, the variation in radius ratio for bubble B_1 is greater in the double-bubble environment. At γ_1 = 3, the peak radius ratio in a dual-bubble environment reaches 28.1, an increase of 31.0% compared to that in a single-bubble environment. Similarly, under identical parameters, the bubble oscillation period is significantly prolonged in the double-bubble environment, and the dual-peak phenomenon occurs.

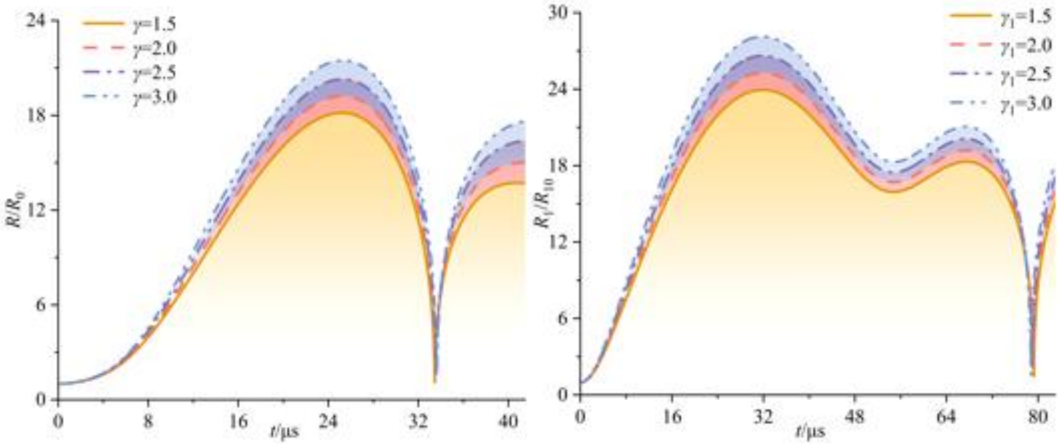

(a) Single-bubble environment (b) Double-bubble environment

Figure 14. Evolution of bubble radius ratio at different dimensionless distances.

Figure 15 shows the collapse-induced pressure field distribution of bubble B_1 at different dimensionless distances in the single-bubble and double-bubble environments, respectively. Figure 15 shows that the instantaneous shock pressure during bubble collapse increases with the dimensionless distance in both single- and double-bubble environments. For a given initial radius, the shock-wave pressure is higher in the double-bubble environment. Correlating with Figure 14, a larger dimensionless distance in a single-bubble environment intensifies oscillations of the radius ratio, indicating elevated bubble wall velocity and acceleration. Greater velocity and acceleration generate more intense bubble oscillations and the resulting collapse pressure.

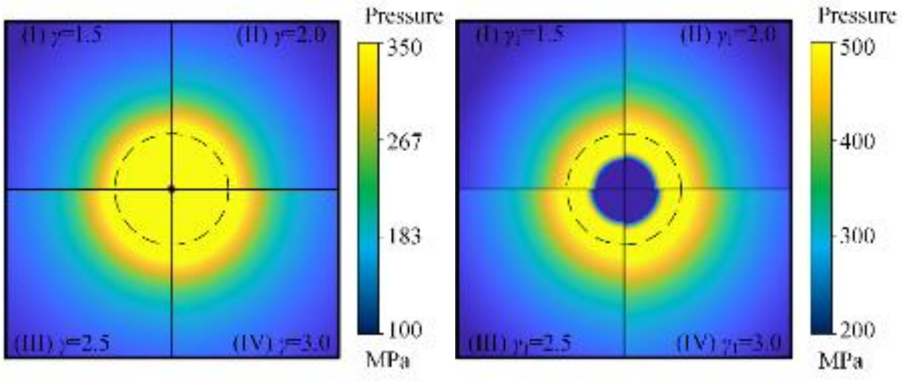

(a) Single-bubble environment (b) Double-bubble environment

Figure 15. Pressure field generated by bubble B_1's collapse at different dimensionless distances

Figure 16 presents wall impact pressure P_{wall} at different dimensionless distances γ for single-bubble and double-bubble environments, respectively. Figure 16 shows that the wall impact pressure P_{wall} decreases with increasing dimensionless distance in both single-bubble and double-bubble environments. In a single-bubble environment at γ = 3.0, the maximum P_{wall} is 383.8 MPa, representing a 10.7% increase over that at γ = 1.5. In a double-bubble environment at γ_1=3.0, the maximum P_{wall} is 482.2 MPa, representing a 12.2% increase over that at γ_1=1.5. Additionally, the maximum P_{wall} values are consistently higher in the double-bubble environment. At dimensionless distance γ=1.5, the maximum P_{wall} is 482.2 MPa in the double-bubble environment, representing a 20.4% increase. Despite lower collapse-induced shock pressures at smaller dimensionless distances, reduced dimensionless distances correspond to shorter bubble-wall distances. Because of this closeness, shock waves travelling toward the wall lose less energy, leading to a higher P_{wall} upon impact. As shown in Figure 16, increasing γ makes the time to reach the peak of P_{wall} longer for single-bubble but shorter for double-bubble, which is consistent with Yin et al. [40] and Han et al. [41]. The reason lies in different physical mechanisms. In the single-bubble environment, a larger γ increases the bubble-wall distance, so shock waves take longer to arrive. In the double-bubble environment, a larger γ leads to more violent radius oscillations (Figure 14), thereby producing stronger shock waves. The faster propagation of these waves compensates for the longer distance, allowing the P_{wall} peak to occur sooner.

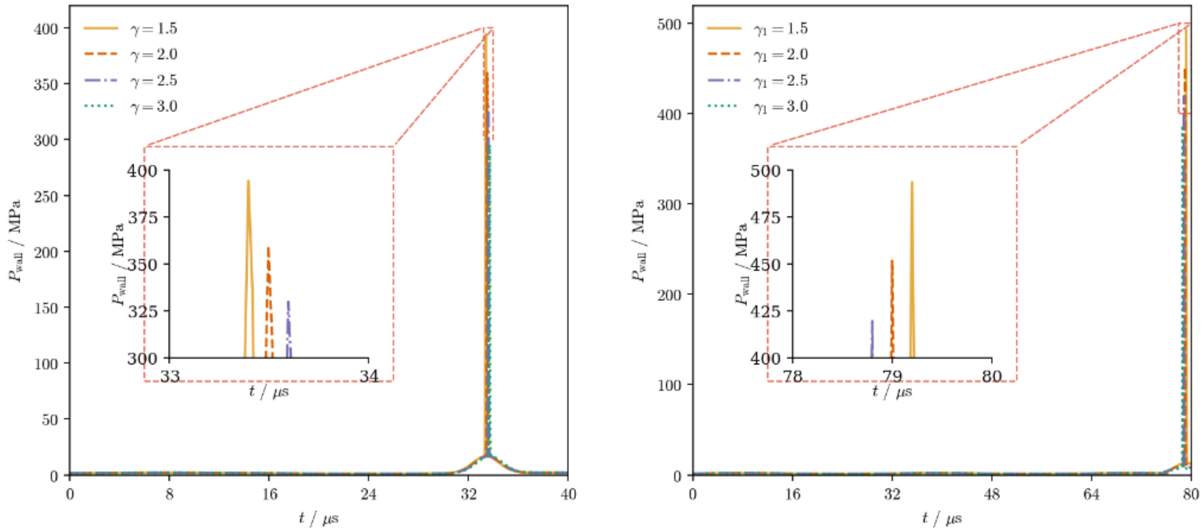

(a) Single-bubble environment (b) Double-bubble environment

Figure 16. Wall impact pressure at different dimensionless distances

3.5 Influence Of Inter-Bubble Distance

In a double-bubble environment, the distance between the two bubbles directly influences the radiated pressures coming from both the neighbouring bubble and its mirror-image counterpart. As a result, the bubble-radius variations and collapse-pressure distributions are altered. Set the initial bubble radius $R_{10} = R_{20}$ =10 µm, the ultrasonic amplitude A = 5 µm, the dimensionless distances $\gamma_1 = \gamma_2$ =1.5, and the inter-bubble spacing L=60, 80, 100, and 120 µm. Figure 17 shows the evolution of the radius ratio R_1/R_{10} as a function of inter-bubble distance. Figure 17 reveals an inverse relationship between the inter-bubble distance L and the bubble radius ratio in a double-bubble environment. When L=60 µm, the peak radius ratio reaches 25.8, which is 12.0% higher than the value of 22.7 at L=120 µm. A larger L reduces the radiation pressure from bubble B_2 and its mirrored bubble B_2', thereby lowering the external pressure on bubble B_1. This leads to a smaller pressure difference across the bubble interface, which in turn reduces the bubble wall velocity and acceleration, making the radius changes more moderate. Consequently, a smaller L produces a larger radius ratio.

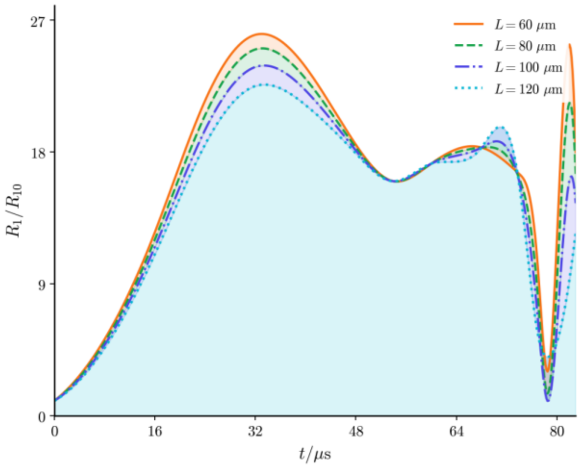

Figure 17. Evolution of bubble radius ratio at different inter-bubble distances

Figure 18 presents the pressure field distribution generated by the collapse of bubble B_1 at different inter-bubble distances in the double-bubble environment. Figure 18 shows that the collapse-induced pressure increases as the inter-bubble distance L decreases in the double-bubble environment. Correlating with Figure 17 reveals that smaller inter-bubble distance leads to more pronounced radius ratio oscillations, indicating elevated bubble wall velocity and acceleration. Increased velocity and acceleration generate greater collapse pressure. Consequently, reduced inter-bubble distances result in stronger collapse shock waves. The wall impact pressures under different inter-bubble distances are presented in Figure 19. Figure 19 illustrates that the wall impact pressure P_{wall} increases as the inter-bubble distance *L decreases*. At L=120 μm, the maximum P_{wall} is 457.1 MPa, while at *L*=60 μm, it reaches 563.3 MPa, representing an increase of 18.9% relative to the 120 μm case. As shown in Figure 18, larger inter-bubble distances decrease collapse pressure, thereby reducing wall impact pressure.

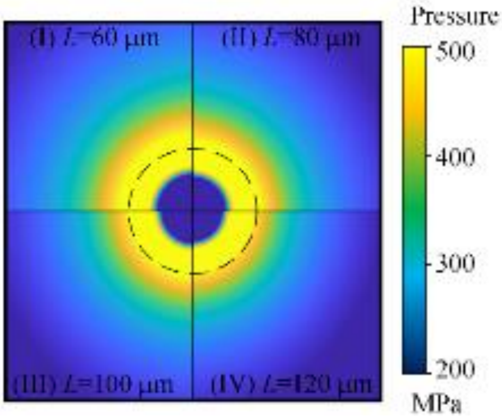

Figure 18. Pressure field generated by bubble B_1's collapse at different inter-bubble distances

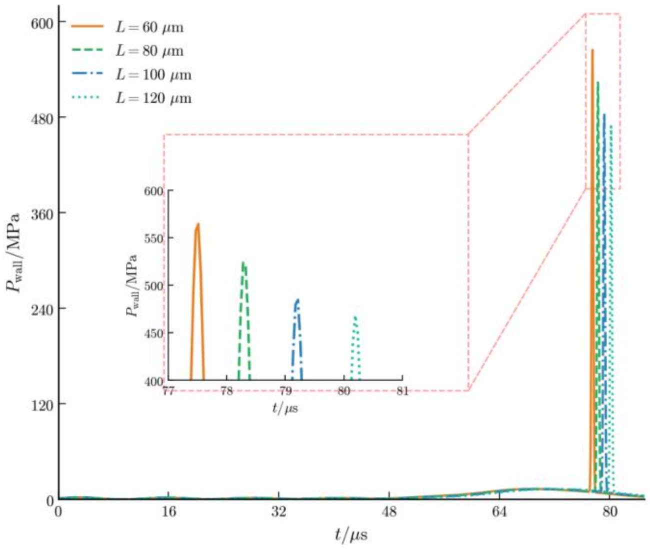

Figure 19 Wall impact pressure at different inter-bubble distances

4. Conclusions

Compared with single-bubble collapse, the synergistic effect in double-bubble collapse intensifies oscillations in bubble-radius ratio and significantly elevates peak shock pressure by up to 23.6%. This interaction also prolongs the oscillation period and induces dual peaks. Key parameters influencing cavitation–initial bubble radius, ultrasonic amplitude, dimensionless distance, and inter-bubble distance–collectively govern collapse dynamics. Smaller initial bubble radius, larger ultrasonic amplitude, smaller dimensionless distance, and smaller inter-bubble distance amplify wall impact pressure. Experimentally derived inverse wall pressures align with analytically predicted values, with an average error of 6.8%, validating the bubble dynamics and pressure field models. Compared to the single-bubble environment, experimentally inverse-derived wall impact pressures in the double-bubble environment showed maximum and minimum enhancements of 23.6% (at an amplitude of 4 μm) and 12.6% (at an amplitude of 3 μm), respectively, confirming the enhancement effect of coupled double-bubble collapse. This study elucidates the interaction mechanism between two bubbles and the effects of processing parameters on this interaction. It provides both a theoretical basis and the capability for predictive control and optimal utilisation of cavitation effects in USR. Future work may introduce fluid viscosity, non-spherical collapse, variable initial radii/positions, and Bjerknes forces to further enhance predictive accuracy.

Acknowledgements

The authors gratefully acknowledge the support provided by Henan Polytechnic University for this project.

Funding

This work was supported by the Key Research and Development and Promotion Program in Henan Province (No. 252102221028).

Declaration of Competing Interest

The author declares no conflicts of interest.

CRediT Authorship Contribution Statement

Hongbo Li: Methodology; Investigation; Validation; Data curation; Writing – original draft
Jianxin Zheng: Conceptualisation; Methodology; Writing – review & editing; Supervision; Project administration; Funding acquisition
Xiao Yu: Validation; Data curation; Writing – review & editing
Junhua Li: Validation; Data curation; Writing – review & editing
Yanyan Yan: Validation; Data curation; Writing – review & editing
Shen Niu: Validation; Data curation; Writing – review & editing

Availability of Data and Materials

The datasets generated and/or analysed during the current study are available from the corresponding author on reasonable request.

Ethics Declarations

This study did not involve human participants or animals. Ethical approval was therefore not required.

Generative Artificial Intelligence Declarations

The authors claim that artificially intelligent-assisted technologies, such as generative AI, were not used to generate content, ideas, or theories. We have just utilised AI to enhance readability and refine the language. This was used with extreme human control and oversight. The authors take full responsibility for reviewing and approving the content.

References

[1] J. Zheng, Y. Shang, Y. Guo, H. Deng, L. Jia, “Analytical model of residual stress in ultrasonic rolling of 7075 aluminum alloy,” *Journal of Manufacturing Processes*, vol. 80, pp. 132-140, 2022.

[2] J. Tong, H. Tao, S. Yang, Y. Ye, H. Zhai, X. Li, et al., “Modeling and experimental validation of residual stresses on the surface of TC4 titanium alloy by eccentric ultrasonic surface rolling process,” *International Journal of Precision Engineering and Manufacturing*, vol. 26, pp. 1335-1355, 2025.

[3] L. Huang, L. Yi, L. Wang, F. Xu, M. Zhou, S. Xia, “Effect of ultrasonic surface rolling process on wear behavior of Mg-15Gd-1Zn-0.4Zr alloy,” *Journal of Materials Engineering and Performance*, vol. 34, pp. 11827–11840, 2025.

[4] S. Žagar, H. Soyama, B. Markoli, I. Naglič, R. Šturm, “Enhancing the surface strength of magnesium alloy AZ80 through cavitation peening,” *Materials & Design*, vol. 255, p. 114229, 2025.

[5] J. Li, J. Zheng, L. Jia, H. Li, “Residual stress and microstructure evolution of 7075 aluminum induced by ultrasonic surface rolling coupled with cavitation,” *Journal of Materials Engineering and Performance*, vol. 34, pp. 24090–24102, 2025.

[6] S. Chuai, X. Zhu, L. Ye, Y. Liu, Z. Wang, F. Li, “Study on the mechanism of ultrasonic cavitation effect on the surface properties enhancement of TC17 titanium alloy,” *Ultrasonics Sonochemistry*, vol. 108, p. 106957, 2024.

[7] J. Chen, H. Liu, H. Yu, K. Wang, C. Kang, G. Liu, et al. “Microscopic structure and hydrophily/ hydrophobicity of AZ31B magnesium alloy surface by ultrasonic cavitation treatment,” *Wear*, vol. 572, p. 206046, 2025.

[8] F. Bai, L. Wang, K. Yang, Z. He, C. Liu, J. Twiefel, “A novel inner surface enhancement method for holes utilizing ultrasonic cavitation,” *Ultrasonics*, vol. 115, p. 106453, 2021.

[9] J. B. Keller, M. Miksis, “Bubble oscillations of large amplitude,” *The Journal of the Acoustical Society of America*, vol. 68, pp. 628-633, 1980.

[10] F. R. Gilmore, The growth or collapse of a spherical bubble in a viscous compressible liquid, Technical Report 26-4, Hydrodynamics Laboratory, California Institute of Technology, Pasadena, CA, USA, 1952.

[11] L. Rayleigh, “On the pressure developed in a liquid during the collapse of a spherical cavity,” *The London, Edinburgh, and Dublin Philosophical Magazine and Journal of Science*, vol. 34, pp. 94-98, 1917.

[12] S. S. Alsaeed, S. Singh. “Insights into coupling effects of double light square bubbles on shocked hydrodynamic instability,” *Physica D: Nonlinear Phenomena*, vol. 476, p. 134646, 2025.

[13] Y. Zhao, S. Jiang, X. Wang, W. Guo, G. Zhao, F. Zhao, et al, “Study on the collapse process of double cavitation bubble based on coarse-grained force field,” *Journal of Molecular Liquids*, vol. 429, p. 127517, 2025.

[14] K. D. Hattori, T. Yamamoto, “Mass transfer of acoustic cavitation bubbles in multi-bubble environment,” *Ultrasonics Sonochemistry*, vol. 115, p. 107295, 2025.

[15] R. Liu, J. Hu, Y. Wu, S. Chen, C. Wang, R. Mo, et al, “Manipulation mechanisms of bubble aggregation and evolution in inertial cavitation fields,” *Ultrasonics Sonochemistry*, vol. 119, p. 107384, 2025.

[16] Z. Lv, R. Hou, Z. Zhang, Z. Fan, “Effect of ultrasonic vibration on cavitation erosion of aluminum oxide in fluid jet machining,” *The International Journal of Advanced Manufacturing Technology*, vol. 111, pp. 2911-2918, 2020.

[17] C. Guo, J. Liu, X. Li, S. Yang, “Effect of cavitation bubble on the dispersion of magnetorheological polishing fluid under ultrasonic preparation,” *Ultrasonics Sonochemistry*, vol. 79, p. 105782, 2021.

[18] J. Zheng, Y. Guo, L. Zhu, H. Deng, Y. Shang, “Cavitation effect in two-dimensional ultrasonic rolling process,” *Ultrasonics*, vol. 115, p. 106456, 2021.

[19] X. Ye, X. Yao, R. Han, “Dynamics of cavitation bubbles in acoustic field near the rigid wall,” *Ocean Engineering*, vol. 109, pp. 507-516, 2015.

[20] C. Guo, J. Wang, X. Li, S. Yang, W. Li, “Velocity characteristics of microjets generated by double bubbles near a rigid wall under ultrasound,” *Chemical Engineering and Processing-Process Intensification*, vol. 199, p. 109765, 2024.

[21] Y. Tomita, A. Shima, “On the behavior of a spherical bubble and the impulse pressure in a viscous compressible liquid,” *Bulletin of JSME*, vol. 20, pp. 1453-1460, 1977.

[22] E. Sonde, T. Chaise, N. Boisson, D. Nelias, “Modeling of cavitation peening: Jet, bubble growth and collapse, micro-jet and residual stresses,” *Journal of Materials Processing Technology*, vol. 262, pp. 479-491, 2018.

[23] J. Liu, L.u Wang, X. Liu, “Implementation and validation of a cavitation model with bubble inertia second-order term and non-condensable gas effects,” *International Journal of Multiphase Flow*, vol. 195, p. 105524, 2026.

[24] Y. Zhang, X. Lu, J. Hu, J. Yu, Y. Zhang,” Experimental and numerical research on jet dynamics of cavitation bubble near dual particles,” *Ultrasonics Sonochemistry*, vol. 112, p. 107168, 2025.

[25] J. Li, J. Zheng, Y. Shang, “Shock wave and microjet produced by bubble collapse in cavitation ultrasonic surface rolling,” *Journal of Mechanical Engineering Science*, vol. 239, pp. 4443–4460, 2025.

[26] C. Kaufhold, F. Pöhl, S. Mottyll, R. Skoda, W. Theisen, “Numerical simulation of the deformation behavior of metallic materials under cavitation induced load in the incubation period,” *Wear*, vol. 376, pp. 1138-1146, 2017.

[27] X. Wang, Q. Mi, Z. Yang, “Effect of multiple cavitation bubble configurations on the collapse behavior and the wall damage,” *Langmuir*, vol. 42, pp. 6773–6784, 2026.

[28] T. Qu, J. Luo, W. Xu, J. Li, G. Fu,” Experimental investigation on the meso-mechanisms of cavitation erosion pit development under different ambient pressures,” *Wear*, vol. 591, p. 206608, 2026.

[29] I. Tzanakis, D.G. Eskin, A. Georgoulas, D.K. Fytanidis,” Incubation pit analysis and calculation of the hydrodynamic impact pressure from the implosion of an acoustic cavitation bubble,” *Ultrasonics Sonochemistry*, vol. 21, pp. 866-878, 2014.

[30] F. Reuter, C. Deiter, C.Ohl, “Cavitation erosion by shockwave self-focusing of a single bubble,” *Ultrasonics Sonochemistry*, vol. 90, p. 106131, 2022.

[31] C. Guo, X. Zhu, J. Wang, G. Liu, “Dynamics comparison analysis of the vibration system of single and double cavitation bubbles under ultrasonic honing,” *Journal of Vibration and Shock*, vol. 35, pp. 182-187, 2016.

[32] J. Luo, Z. Niu, “Jet and shock wave from collapse of two cavitation bubbles,” *Scientific Reports*, vol. 9, p. 1352, 2019.

[33] Y. Yang, M. Shan, Y. Zhang, H. Li, X. Kan, Q. Han, “Numerical investigation of acoustic cavitation behavior and cavitation-induced thermal effects using lattice Boltzmann method,” *Computers & Fluids*, vol. 279, p. 106325, 2024.

[34] Y. Liu, X. He, C. Huang, J. Zhang, “Interaction dynamics between cavitation bubbles and compressible air bubbles in an infinite domain,” *International Journal of Heat and Mass Transfer*, vol. 249, p. 127214, 2025.

[35] Y. Yang, J. Tu, M. Shan, Z. Zhang, C. Chen, H. Li, “Acoustic cavitation dynamics of bubble clusters near solid wall: A multiphase lattice Boltzmann approach,” *Ultrasonics Sonochemistry*, vol. 114, p. 107261, 2025.

[36] X. Zhang, F. Li, C. Wang, R. Mo, J. Hu, J. Guo, et al, “Effects of translational motion on the Bjerknes forces of bubbles activated by strong acoustic waves,” *Ultrasonics*, vol. 126, p. 106809, 2022.

[37] Q. Nguyen, D. N. Hai, T. Nguyen, V. Nguyen, J. Hwang, W. Park, “Numerical analysis of pressure propagation emitted by collapse of a single cavitation bubble near an oscillating wall,” *CMES-Computer Modeling in Engineering and Sciences*, vol. 145, pp. 3433-3452, 2025.

[38] X. Yang, C. Liu, J. Li, Y. Yang, M. Zhao, C. Hu, “Numerical study of liquid jet and shock wave induced by two-bubble collapse in open field,” *International Journal of Multiphase Flow*, vol. 168, p. 104584, 2023.

[39] K. Choi, H. Kim, C. Kim, “Effects of phase change in double underwater explosion bubbles,” *Ocean Engineering*, vol. 308, p. 118254, 2024.

[40] J. Yin, Y. Zhang, X. Qi, L. Tian, D. Gong, M. Ma, “Numerical investigation of the cavitation bubble near the solid wall with a gas-entrapping hole based on a fully compressible three-phase model,” *Ultrasonics Sonochemistry*, vol. 98, p. 106531, 2023.

[41] W. Han, Z. Xu, Y. Hao, J. Ren; W. Li; Z. Gu, “Study on the dynamic characteristics of the impact loads in a near-wall double-cavitation bubble collapse,” *Processes*, vol. 11, no. 11, p. 1805, 2023.